

1 **Retrieval of convective available potential energy from INSAT-3D measurements:**
2 **comparison with radiosonde data and its spatial-temporal variations**

3 *Uriya Veerendra Murali Krishna¹, Subrata Kumar Das^{1*}, Kizhathur Narasimhan Uma², and*
4 *Govindan Pandithurai¹*

5
6 ¹Indian Institute of Tropical Meteorology, Pune-411008, India

7 ²Space Physics Laboratory, Vikram Sarabhai Space Centre, Trivandrum-695022, India

8 *Correspondence to Subrata Kumar Das (skd_ncu@yahoo.com)

9

10 **Abstract:**

11 Convective available potential energy (CAPE) is a measure of the amount of energy
12 available for convection in the atmosphere. The satellite-derived data over the ocean and land
13 is used for a better understanding of the atmospheric stability indices. In this work, an attempt
14 is made for the first time to estimate CAPE from high spatial and temporal resolution
15 measurements of the INSAT-3D over the Indian region. The estimated CAPE from the
16 INSAT-3D is comprehensively evaluated using radiosonde derived CAPE and ERA-Interim
17 CAPE. The evaluation shows that the INSAT-3D CAPE reasonably correlated with the
18 radiosonde derived CAPE; however, the magnitude of CAPE shows higher values. Further,
19 the distribution of CAPE is studied for different instability conditions (different range of
20 CAPE values) during different seasons over the Indian region. In addition, the diurnal and
21 seasonal variability in CAPE is also investigated at different geographical locations to
22 understand the spatial variability with respect to different terrains.

23

24 **Keywords:** CAPE; Diurnal; INSAT-3D; Instability; Monsoon

25 **1. Introduction**

26 Convective available potential energy (CAPE; Moncrieff and Miller, 1976) is a
27 measure of convective potential in the atmosphere that incorporates the instability and
28 moisture ingredients (Johns and Doswell, 1992). Climatology of CAPE provides valuable
29 information for severe weather forecasting. CAPE can also be used as a potential indicator of
30 climate change (Gettelman et al., 2002; DeMott and Randall, 2004; Riemann Campe et al.,
31 2008; Murugavel et al., 2012; Brooks, 2013). Variability in CAPE can also affect the
32 temperature field in the upper troposphere (Gaffen et al., 1991; Dhaka et al., 2010). For
33 example, Dhaka et al. (2010) studied the relationship between seasonal, annual, and large-
34 scale variations in CAPE and the solar cycle on the temperature at 100 hPa pressure level
35 using daily radiosonde data for the period 1980–2006 over the Indian region. They showed
36 that the increase in CAPE was associated with the decrease in temperature at 100-hPa
37 pressure level on all time scales.

38 The convective schemes in general circulation models use CAPE as a variable for
39 calculating convective heating (e.g., Arakawa and Schubert, 1974; Moncrieff and Miller,
40 1976; Washington and Parkinson, 2005). Many of the cumulus parameterization schemes
41 make use of CAPE in constructing closures (Donner and Phillips, 2003). The diurnal
42 variation of CAPE is of primary importance for understanding the sensitivity of convection
43 schemes in the model to produce the diurnal cycle of precipitation (Lee et al., 2007). The
44 reliability of model-simulated temporal and spatial variations in CAPE is an important
45 indicator of model performance, particularly in the tropics (Gettelman et al., 2002). Also, the
46 seasonal and diurnal changes in CAPE are important for models to provide validation of their
47 capacity to simulate future changes in the tropical climate. The above studies conclude that
48 the estimation of CAPE is imperative, not only for assessing the conditional instability of the

49 atmosphere and for the convective parameterization, but also for the studies related to
50 climatic change.

51 Most of the earlier studies on CAPE are based on radiosonde observations. Globally,
52 the radiosonde is launched twice a day, 0000 and 1200 UTC. This limits the studies on CAPE
53 at diurnal scales. It is also to be noted that the radiosonde observations are limited to land,
54 and are very sparse over the oceans. Reanalysis datasets fill these gaps; however, their spatial
55 resolution is poor and most of the time the data accuracies do not match with the standard
56 techniques. The satellite observations are the only solutions to have regular observations of
57 CAPE with high spatial resolution across the globe. With the availability of satellite
58 measurements, several studies were carried out on CAPE. Narendra Babu et al. (2010)
59 studied the seasonal and diurnal variations in CAPE over land and oceanic regions using one
60 year of observations from the FORMOSAT mission 3/Constellation Observing System for
61 Meteorology, Ionosphere, and Climate (COSMIC/FORMOSAT-3) Global Positioning
62 System (GPS) Radio Occultation (GPS-RO) measurements. Santhi et al. (2014) estimated
63 various stability indices using COSMIC GPS-RO profiles and the uncertainty in estimating
64 these stability indices. They also studied the diurnal variation of these stability indices over
65 Gadanki, India. In order to study the diurnal variation of stability indices, they integrated the
66 data over a season as the occultations were sparse and hence not adequate to study on daily
67 scale. This limitation of under sampling can be overcome by the use of geostationary
68 satellites. These geostationary satellite measurements provide near-continuous monitoring of
69 the atmosphere with better spatial coverage, which is helpful in nowcasting of convection
70 (Koenig and de Coning, 2009). Siewert et al. (2010) discussed the advantages of the
71 METEOSAT Second Generation (MSG) system in deriving the instability indices and to
72 predict the convection initiation over the Central Europe and South Africa. Using the MSG
73 satellite measurements, de Coning et al. (2011) derived a new convection indicator, the

74 combined instability index which can calculate the probability of convection over the South
75 Africa. They showed that the combined instability index can predict the convection better
76 than the individual instability indices like K-index, total totals index etc. Jewett and
77 Mecikalski (2010) developed an algorithm to derive convective momentum fluxes from the
78 Geostationary Operational Environmental Satellite (GOES) measurements. The advantage of
79 this algorithm is that it can be used in any convective environment.

80 Recently, the Indian Space Research Organization (ISRO) launched the Indian
81 National Satellite System (INSAT-3D), which is a geostationary satellite that provides the
82 profile of temperature and relative humidity with high temporal and spatial resolution.
83 Several researchers evaluated the temperature and relative humidity measurements from the
84 INSAT-3D. Mitra et al. (2015) evaluated the INSAT-3D temperature and moisture retrievals
85 up to 100 hPa with GPS sonde observations for the period January-May 2014. They observed
86 that the INSAT-3D measurements compare better with GPS sonde observations at middle
87 levels (from 900 hPa to 500 hPa). The assessment of the quality of temperature and water
88 vapour obtained from the INSAT-3D with in-situ, satellite, and reanalysis datasets by Ratnam
89 et al. (2016) revealed that the INSAT-3D measurements agree well with the GPS sonde
90 observations, satellite measurements and reanalysis datasets below 25°N. The temperature
91 difference was 0.5K with a standard deviation of about 1K, and for humidity, a dry bias (20-
92 30%) was observed between INSAT-3D and GPS sonde observations. Hence, these satellite
93 measurements also suffer from some inherent shortcomings and have biases and random
94 errors. Therefore, it is essential to evaluate the satellite products with conventional
95 measurements to quantify the direct usability of these products.

96 The objective of the present study is to calculate CAPE from high spatial and
97 temporal resolution measurements of INSAT-3D over the Indian region and its performance
98 assessment. To date there are no studies utilizing such high-resolution data for such a long

99 period to evaluate and understand the variability of CAPE. Hence, this study provides the
100 direct usability of INSAT-3D data sets in the numerical weather prediction models for
101 nowcasting of thunderstorms and for severe weather conditions, which is lacking over the
102 Indian region. In this work, we first attempted to validate the estimated CAPE from the
103 INSAT-3D measurements with that of radiosonde measurements over different stations in
104 India. In general, there are many profiles that do not reach the ground level in the INSAT-3D
105 measurements. Hence, different statistical indices are calculated to assess the detectability of
106 INSAT-3D derived CAPE over these regions. Secondly, the diurnal variation of CAPE is
107 studied at different regions in India. Finally, the seasonal mean CAPE is estimated over the
108 Indian region. The paper is organized as follows. Section 2 provides the details of the data
109 sets used. Section 3 discusses the methodology adopted to estimate the CAPE. Section 4
110 provides the results and discussion. Finally, summary of the present study is provided in
111 section 5.

112

113 **2. Database**

114 **2.1. *INSAT-3D***

115 In the present study, three years (01 April 2014 - 31 March 2017) of measurements
116 obtained from the INSAT-3D are used to estimate CAPE over the Indian region and assess
117 the estimation against radiosonde measurements. The INSAT is a series of multipurpose
118 geostationary satellites launched by the ISRO, India. The INSAT-3D, which is considered to
119 be the advanced version of all the other INSAT series satellites, is a multipurpose
120 geosynchronous spacecraft with main meteorological payloads (imager and sounder)
121 launched on 26 July 2013. The main objective of the mission is to monitor the earth and
122 ocean continuously and also provide data dissemination capabilities. The INSAT-3D also

123 provides an operational, environmental and storm warning system to protect life and
124 property.

125 The INSAT-3D spacecraft carries two meteorological payloads: (i) Imager (optical
126 radiometer) provides high-resolution images of mesoscale phenomena in the visible and
127 infrared (IR) spectral bands (0.55 to 12.5 μm) and (ii) Sounder has one visible and 18 IR (7 in
128 long-wave IR, 5 in mid-IR, and 6 in short-wave IR) channels. The sounder measures the
129 irradiance and provide profiles of temperature, water vapour and integrated ozone over the
130 Indian landmass and surrounding ocean every hour and over the whole of the Indian Ocean
131 every 6 hours with a spatial resolution of 0.1° . For the present study, temperature and water
132 vapour data collected from the INSAT-3D sounder during the clear (cloud free) conditions.
133 These dataset are interpolated to 0.25° spatial resolution and are used to estimate the CAPE
134 over the Indian region.

135 **2.2. Radiosonde**

136 Upper air radiosonde profiles are downloaded from the University of Wyoming
137 website (<http://weather.uwyo.edu/upperair/sounding.html>). Radiosonde data are usually
138 available at 0000 and 1200 UTC regularly to monitor the thermodynamic state of the
139 atmosphere by the National Weather Service. For the present study, the data collected for 20
140 stations (black dots in Fig. 1) for the period from 01 April 2014 to 31 March 2017 are used to
141 assess the INSAT-3D estimated CAPE. The values of CAPE reported in this paper are taken
142 directly from the data provided by the University of Wyoming.

143 **2.3. ERA-Interim Reanalysis**

144 The reanalysis dataset used in this study are from the ERA-Interim project (Dee et al.,
145 2011). The ERA-Interim is the latest global atmospheric reanalysis produced by the European
146 Centre for Medium-Range Weather Forecasts (ECMWF), which envisaged preparing a future
147 reanalysis project that will span the entire twentieth century. The ERA-Interim data are

148 available in near-real time from 1 January 1979 onwards. The ERA-Interim generates gridded
149 data, including a large variety of surface parameters that describe the weather as well as land
150 surface and ocean conditions at the 3-hourly and 6-hourly interval. The present study utilizes
151 the CAPE derived from the ERA-Interim dataset. The data are extracted over the Indian
152 region at 0000 and 1200 UTC for each day between 01 April 2014 and 31 March 2017. The
153 spatial resolution of the data utilized is $0.25^{\circ} \times 0.25^{\circ}$.

154

155 **3. Estimation of CAPE**

156 To calculate the CAPE, the vertical profiles of temperature and water vapour are
157 taken from the INSAT-3D measurements. For many years, a debate has existed in the
158 literature regarding the most meaningful way to calculate CAPE and how to interpret the
159 result. The most important methods of calculating CAPE is (1) pseudoadiabatic CAPE in
160 which CAPE is estimated after assuming that all the condensate has fallen out of the air
161 parcel and (2) reversible CAPE in which it is assumed that the condensate remains within the
162 parcel. In the present study, the pseudoadiabatic algorithm is used to calculate CAPE.
163 Further, CAPE is very sensitive to near-surface temperature and humidity (Gartzke et al.,
164 2017), which are known to vary spatially. However, Ratnam et al. (2016) found that the
165 variability of the atmospheric state within the INSAT-3D footprint sampled by the radiosonde
166 had little bias over the Indian region. They also reported that the difference in temperature
167 between INSAT-3D and ERA-Interim reanalysis datasets lies within 1K and a dry bias of 5–
168 10% was found in the lower and mid-troposphere relative humidity when compared with the
169 ERA-Interim reanalysis datasets. In this scenario, it is assumed that the spatial sampling
170 mismatch may not affect much in the calculation of CAPE and hence are neglected in the
171 present study. In addition, only cases with radiosonde profiles having CAPE greater than 0 J

172 kg^{-1} are included in the analysis. This threshold is used to eliminate the large number of zero
173 CAPE values.

174 The integration of the buoyancy of the air parcel from the level of free convection
175 (LFC) to equilibrium level (EL) gives the measure of CAPE.

$$CAPE = \int_{LFC}^{EL} \frac{g(T_{vp} - T_{ve})}{T_{ve}} dZ \quad (1)$$

176

177 Where, T_{vp} is the virtual temperature of the air parcel and T_{ve} is the virtual temperature of the
178 environment, g is the acceleration due to gravity. The LFC is situated above the lifting
179 condensation level (LCL) and at that level, the parcel temperature is greater than the
180 environmental temperature. This is calculated by lifting the air parcel moist adiabatically. The
181 EL is situated above the LFC and at this level, the parcel temperature is less than or equal to
182 the environment temperature. At EL, the air parcel attains stability and the convection stops.
183 Under stable environmental conditions, the LFC and EL will not be present. The procedure to
184 estimate CAPE is similar as discussed in Uma and Das (2017).

185 The error in estimating the CAPE is determined by applying the standard error
186 propagation formula (Bevington and Robinson, 1992). The error in the CAPE calculation
187 depends on the temperature and water vapour retrievals. In this study, an error of 5% in the
188 measured relative humidity and temperature corresponds to an error of 8% in the calculated
189 CAPE from the INSAT-3D measurements.

190

191 **4. Results and Discussions**

192 Three years of data collected from the INSAT-3D measurements are utilized to
193 estimate CAPE over the Indian region. These estimates are compared with the radiosonde
194 derived CAPE at 0000 and 1200 UTC along with the ERA-Interim reanalysis CAPE data.

195 **4.1. Comparison of INSAT-3D CAPE with radiosonde and ERA-Interim CAPE**

196 In this work, 20 stations are selected for which the radiosonde profiles are available
197 during the study period (location shown in Fig. 1). Table 1 provide the details of the stations
198 considered along with the total number of data available from INSAT-3D measurements
199 during four seasons (winter: December to February; pre-monsoon: March to May; monsoon:
200 June to September; and post-monsoon: October and November). Fig. 2 shows the correlation
201 coefficient along with the number of data points used in the analysis for the comparison
202 between estimated CAPE from the INSAT-3D measurements, ERA-Interim CAPE, and
203 radiosonde derived CAPE. Here, the comparison is performed only when the INSAT-3D and
204 radiosonde CAPE as well as INSAT-3D and ERA-Interim CAPE greater than zero. From this
205 figure, it is noticed that the INSAT-3D estimated CAPE shows better correlation with
206 radiosonde CAPE compared to the ERA-Interim CAPE. In general, the coastal stations show
207 a higher correlation coefficient than that of the other stations for the INSAT-3D estimated
208 CAPE. All the coastal stations show a correlation higher than 0.6 except Trivandrum. The
209 correlation coefficient is as high as 0.84 for Chennai among all the stations. The correlation
210 values are lower for the stations located near the foothills of Himalayas and north-east (NE)
211 regions of India. A weak correlation of 0.31 is found for Delhi. For the ERA-Interim data,
212 INSAT-3D CAPE shows less correlation coefficient for all the stations except Amini Divi
213 compared to radiosonde CAPE. Even in the ERA-Interim CAPE, the coastal stations show
214 better correlation compared to other stations. The ERA-Interim CAPE shows a higher
215 correlation for Minicoy and the correlation is minimum for Delhi. This result suggests that
216 the INSAT-3D CAPE measurements agree well with the radiosonde measurements.

217 To elucidate the consistency of INSAT-3D estimated CAPE against the ERA-Interim
218 CAPE, the bias in the measurements of INSAT-3D and ERA-Interim with the radiosonde is
219 presented in Fig. 3. The bias evaluates the size of the difference between the two datasets.
220 The positive (negative) value of bias indicates the overestimation (underestimation) of the

221 satellite/reanalysis measurements. The INSAT-3D estimated CAPE shows small and positive
222 bias for most of the stations considered in the study. Among all the stations, Hyderabad,
223 Gorakhpur, and Delhi show higher bias, whereas Mumbai shows minimum bias. All the
224 stations show positive bias except Ahmedabad, Dibrugarh, Delhi, Gorakhpur, and Port Blair
225 where the bias is negative and Mumbai shows small negative bias. Whereas, the ERA-Interim
226 CAPE shows negative bias for all the stations indicating the underestimation of CAPE
227 compared to radiosonde measurements. Further, the bias in the estimation of CAPE in the
228 ERA-Interim data is higher for most of the stations. Among all the stations, Gorakhpur shows
229 higher negative bias. From this, it is clear that the INSAT-3D (ERA-Interim) overestimated
230 (underestimated) the CAPE compared to radiosonde measurements. From the above
231 discussion, it can be concluded that the INSAT-3D provides better estimates over coastal
232 regions compared to other regions and also a better comparison with the radiosonde
233 measurements.

234 ***4.2. Statistical indices in the estimation of CAPE from INSAT-3D measurements***

235 Furthermore, to examine the capability of detection of the INSAT-3D sounder, the
236 probability of detection (POD), false alarm ratio (FAR), critical success index (CSI), and
237 accuracy (ACC) are computed on the basis of a contingency table (Table 2). A threshold
238 value of zero is considered for CAPE to be estimated by the satellite measurements. The POD
239 is a measure of the CAPE successfully identified by the satellite product, and FAR gives a
240 proportional measure of the satellite product's tendency to estimate CAPE where none is
241 observed i.e., it gives the CAPE estimates that are incorrectly detected. CSI represents how
242 well the estimated CAPE events correspond to the observed CAPE events. ACC measures the
243 fraction of the correctness in the CAPE estimates. For a perfect satellite-based estimate, the
244 values of POD, FAR, CSI, and ACC should be 1, 0, 1, and 1 respectively. These statistical
245 indices can be calculated as:

246

$$POD = \frac{a}{a + c} \quad (2)$$

247

$$FAR = \frac{b}{a + b} \quad (3)$$

248

$$CSI = \frac{a}{a + b + c} \quad (4)$$

249

$$ACC = \frac{a + d}{a + b + c + d} \quad (5)$$

250

251 Fig. 4(a)-(d) shows the POD, FAR, CSI, and ACC calculated for the INSAT-3D
252 estimated CAPE respectively. Among all the stations, Mumbai shows higher POD whereas
253 Hyderabad shows lower POD. This indicates that the INSAT-3D is unable to detect CAPE
254 over Hyderabad. This may be due to less availability of data and the inability to catch the
255 short-lived convective storms frequently observed over this region. All the coastal stations
256 show higher POD, CSI, and ACC. Cochin shows the highest CSI and ACC, whereas
257 Agarthala and Kolkata have highest FAR. This indicates that the INSAT-3D product
258 performs reasonably well with the higher POD, CSI, and ACC and lower FAR.

259 **4.3. Distribution of CAPE over India**

260 A summary of the frequency distribution of CAPE computed from the INSAT-3D,
261 ERA-Interim and radiosonde measurements for the 20 stations are shown in Fig. 5. The
262 distribution of CAPE shows higher occurrence for lower values. Thus, the CAPE distribution
263 is shifted to lower values in all the three measurements. The INSAT-3D estimated CAPE and
264 ERA-Interim CAPE shows a similar kind of distribution compared to radiosonde CAPE. The

265 distribution of the INSAT-3D estimated CAPE is higher (lower) in the range ~300-1200
266 (1200-3000) J kg^{-1} compared to the radiosonde measurements. The INSAT-3D estimated
267 CAPE matches with the radiosonde CAPE above 3000 J kg^{-1} . The ERA-Interim CAPE
268 distribution shows higher values below 1200 J kg^{-1} . However, the ERA-Interim distribution
269 becomes negligible above 2000 J kg^{-1} . This also shows that for the higher values of CAPE,
270 ERA-Interim underestimates the observations. This may be due to the fact that the spatial
271 resolution of the reanalysis data are coarse compared to the observations. The figure shows
272 that among the two distributions, the INSAT-3D distribution agrees well with the radiosonde
273 distribution.

274 **4.4. Seasonal variation of CAPE**

275 In the present study, the INSAT-3D dataset is divided into four seasons viz., winter,
276 pre-monsoon, monsoon, and post-monsoon to understand the seasonal variations in CAPE
277 over the Indian region. Fig. 6(a)-(d) shows the seasonal mean CAPE estimated from the
278 INSAT-3D measurements during the period from April-2014 to March-2017 over the Indian
279 region. During winter season (Fig. 6a), the mean CAPE is below 500 J kg^{-1} over the land
280 regions. The mean CAPE is relatively higher over the west coast and Arabian Sea (AS) and
281 the parts of northern Bay of Bengal (BoB). This relatively high CAPE over oceans and the
282 western coastal regions may be due to the occurrence of depression and cyclone during the
283 month of December over the oceanic regions. In the pre-monsoon season (Fig. 6b), higher
284 values of CAPE (above 2000 J kg^{-1}) are observed over the AS, BoB and Central India (CI).
285 The pre-monsoon depressions are regular during this time period over surrounding oceanic
286 regions of India. This sustains for few days which results in higher CAPE over these regions.
287 Higher values of CAPE are the causing factors for frequent thunderstorms and deep
288 convection over the Northern and Central India. The Western Ghats has higher CAPE which
289 may be due to the orographic induced deep convection. CAPE is lower over the Southern

290 Peninsular India. Further, the CI, north India (NI) and foothills of Himalayas exhibits higher
291 CAPE compared to other land regions. The north-western parts of India show higher CAPE
292 among other land regions. During the monsoon season (Fig. 6c), the east coast of India, AS,
293 BoB, and foothills of Himalayas shows relatively higher CAPE than the other regions.
294 During the post-monsoon period (Fig. 6d), the northern parts of AS and BoB, east coast of
295 India and west coast of India shows higher values of CAPE and the southern peninsula and
296 eastern regions shows lower CAPE.

297 Further, the spatial distribution of CAPE estimated from the INSAT-3D is studied for
298 different CAPE ranges. The spatial distribution of CAPE provides information on the
299 distribution of extreme weather events over the study region. The estimated CAPE is divided
300 into four categories: weak instability ($<500 \text{ J kg}^{-1}$), moderate instability ($501-1500 \text{ J kg}^{-1}$),
301 strong instability ($1501-3000 \text{ J kg}^{-1}$), and extreme instability ($>3000 \text{ J kg}^{-1}$). The normalized
302 anomaly distribution of CAPE in the four instability conditions during different seasons is
303 provided over the Indian region as shown in Fig. 7. The spatial distribution of CAPE during
304 the weak, moderate, strong, and extreme instability conditions is shown in Fig. 7(a)-(d), 7(e)-
305 (h), 7(i)-(l), and 7(m)-(p) respectively. The top panel is for the winter, second from the top is
306 for the pre-monsoon, third from the top is for the monsoon and bottom panel is for the post-
307 monsoon season. Here, the negative (positive) anomaly indicates the increase (decrease) in
308 CAPE. During winter, the response of weak instability (Fig 7a) is very less over the Indian
309 subcontinent as well as the surrounding oceanic regions. However, the response of winter
310 towards strong and extreme instability is observed over the BoB, Southeast AS, and some
311 parts of the NI. The higher response may be due to the cyclones and depressions that occur
312 over the oceanic regions during December. Over the NI, strong westerlies are observed
313 during the winter, which may result in a dry convection with higher CAPE.

314 The response during pre-monsoon is observed to be higher for strong and extreme
315 instability. The pre-monsoon season is considered to be summer over the Indian subcontinent
316 and it is the favorable season for thunderstorms and deep convection. This could be easily
317 observed in the figure that during extreme instability the whole Indian region is observed to
318 have higher frequencies of CAPE. During monsoon season, the response to weak and
319 moderate instability is more compared to strong and extreme instability. It is observed that
320 the Western Ghats and the surrounding oceanic regions have more frequency of weak and
321 moderate instabilities compared to the other regions. The Western Ghats is generally
322 dominated by the shallow clouds (e.g., Das et al., 2017; Utsav et al., 2017), which results in
323 high response with weak instability as deep convection does not predominantly occur over
324 this region. The monsoon trough region extending from heat low in Pakistan to head BoB
325 respond to strong instability. This trough (core low-pressure region) occurs during the
326 monsoon, which results in heavy rainfall over the Indian subcontinent. Compared to the pre-
327 monsoon, there is little response in strong instability conditions over the oceanic regions.
328 This results in fewer occurrences of deep convection and cyclones (inhibited because of the
329 presence of strong wind shear at 500 hPa) during the monsoon season. In the post-monsoon,
330 the response is much similar to the pre-monsoon during the strong and extreme instability
331 conditions. In post-monsoon, the wind flow over the Indian region is northeasterly which
332 results in more convection over the northwestern and the southern peninsular Indian region.
333 Usually, in October-November months, the deep depression occurs over the Bay of Bengal
334 due to which higher frequency of CAPE is observed. In general, weak instability is
335 predominant during winter season. The moderate instability shows higher occurrence during
336 post-monsoon compared to other seasons. The strong instability condition is more during the
337 monsoon period whereas the occurrence of extreme instability is higher during pre-monsoon
338 months.

339 **4.5. Diurnal variation of CAPE**

340 Fig. 8 shows hourly mean CAPE averaged for three years (2014-2017). A strong
341 diurnal variation in the mean CAPE is observed over different parts of India. A clear land-sea
342 contrast is also observed in the mean CAPE. The CAPE starts building up in the morning
343 (0530 LT=00UTC+0530) over the oceans with land having low values of CAPE. The mean
344 CAPE reaches its maximum at ~1200 LT over the oceans. However, the CAPE starts
345 increasing after 0900 LT over the land and reaches the maximum in the afternoon (between
346 1300 and 1400 LT) and decreases again thereafter. The land-sea contrast in the mean CAPE
347 has disappeared in the evening. Again in the evening, the CAPE increases and a secondary
348 maximum is observed in the midnight over the oceans. Over the tropics, the Indian region is
349 one of the active convective regions. The deep convective clouds form during the daytime
350 over the Indian sub-continent due to solar insolation, which increases the lower tropospheric
351 temperature resulting in convective instability. Uma and Das (2016) have found the lower
352 tropospheric humidity maximum in the afternoon and minimum in the evening hours. The
353 surrounding oceanic regions found to peak in the late evening and midnight. This indicates
354 that the convection peaks in the late afternoon over the land region and evening to midnight
355 over the oceans. These results are consistent with the findings of Dutta and Rao (2001) and
356 Dutta and Kesarkar (2004). These studies revealed that the maximum value of CAPE is
357 observed during nighttime over the BoB and east coast of India. However, this secondary
358 maximum is not observed over the land areas. In contrast, another maximum is observed
359 around 1700 LT over the east coast, west coast and north-west regions of India.

360 To observe the diurnal variation of CAPE over different parts of India, the study
361 region is divided (latitude-wise for uniformity) into six sub-regions as provided in Raut et al.
362 (2009). These regions are: the Arabian Sea (AS; 8-20°N, 65-72°E), Bay of Bengal (BoB; 8-
363 20°N, 80-90°E), South Peninsular India (SP; 8-20°N, 72-80°E), Central India (CI; 20-25°N,

364 73-82°E), North India (NI; 25-35°N, 73-80°E), and Northeast India (NE; 24-29°N, 90-
365 96°E). Fig. 9 shows the diurnal variation of mean CAPE over these sub-regions during four
366 seasons. From this figure, one can observe a bimodal distribution in the mean CAPE over the
367 AS and BoB during the pre-monsoon and monsoon periods (Fig. 9a and b). The primary
368 maximum is observed in the nighttime and the secondary maximum is observed in the
369 afternoon time over these regions. Uma and Das (2016) have also observed bimodal
370 distribution in the relative humidity over the BoB and the Indian Ocean. They found
371 maximum distribution at 1200 and 1500 LT, which is almost similar to that observed in the
372 present study. During Bay of Bengal Monsoon Experiment (BOBMEX) 1999, Dutta and
373 Kesarkar (2004) observed that the CAPE is maximum in the nighttime than in the daytime.
374 Further, the nighttime maximum in the mean CAPE is observed around ~0000 LT over BoB,
375 and AS during the pre-monsoon and monsoon periods. The bimodal distribution in mean
376 CAPE is also observed over the AS and BoB during post-monsoon season. However, the
377 secondary maximum is not much prominent as observed in the pre-monsoon and monsoon
378 periods. The mean CAPE peaks in the afternoon hours over the AS and BoB during winter
379 season.

380 The SP region (Fig. 9c) also shows the similar behavior as that of oceans. The mean
381 CAPE over the SP region maximizes in the afternoon hours. The secondary maximum is also
382 observed in the late night (0000 LT). The mean CAPE in the CI region (Fig. 9d) shows a
383 bimodal distribution during winter, monsoon and post-monsoon seasons. The mean CAPE is
384 at its maximum in the afternoon time. The other maximum is during the nighttime. A
385 noticeable difference is observed in the mean CAPE during the pre-monsoon season. During
386 this period, the CAPE is nearly the same throughout the day. However, this CAPE decreases
387 a little and becomes minimum in the early morning over the CI region. The mean CAPE in
388 the NI region (Fig. 9e) shows a similar diurnal variation as observed over the CI region. The

389 mean CAPE shows little variation during the pre-monsoon months. The other three seasons
390 show bimodal distribution as observed in other regions. However, the magnitude of the mean
391 CAPE is higher in the NI region compared to the CI region. Further, the difference in mean
392 CAPE between primary and secondary maximum is relatively small compared to the other
393 regions. The NE region (Fig. 9f) also shows a bimodal distribution in mean CAPE with the
394 primary maximum in the afternoon hours and the secondary maximum in the late-night
395 during winter, monsoon and post-monsoon seasons. In addition to these two maxima, a third
396 maximum is also observed over the NE region during the pre-monsoon season. The third
397 maximum is observed at ~0900 LT over this region. The third maximum observed in the
398 mean CAPE may be due to the occurrence of pre-monsoon thunderstorms known as
399 Norwesters during the morning over this region.

400 The statistical analysis of CAPE is also attempted over these six regions to understand
401 the variability during different seasons as shown in Fig. 10. The mean, standard deviation
402 along with maximum/minimum with 25, 50 and 70 % occurrence are provided in the figure.
403 During winter, the mean CAPE is higher ($\sim 1600 \text{ J kg}^{-1}$) over the AS compared to that of the
404 BoB ($\sim 1000 \text{ J kg}^{-1}$). Over the land regions, the mean CAPE is found to be less than $\sim 1000 \text{ J}$
405 kg^{-1} . The oceanic regions are found to have higher CAPE during winter compared to that of
406 the continent. The NI and NE have smaller CAPE during winter period. Winter is extremely
407 dry over the Indian region except for the surrounding oceanic regions and south peninsular
408 India, where we observe cyclones/depressions during December, which brings more moisture
409 and heavy rainfall as discussed earlier. During pre-monsoon months, the mean CAPE is
410 higher than $\sim 2000 \text{ J kg}^{-1}$ over all the regions concerned. The pre-monsoon depressions,
411 thunderstorms, deep convection and Norwesters contribute to higher CAPE values over India
412 and surrounding oceanic regions. During monsoon season, the mean CAPE is less than ~ 1500
413 J kg^{-1} over all the regions except the NI where it is about $\sim 2000 \text{ J kg}^{-1}$. The shallow

414 convection dominates during the monsoon season rather than deep convection, which results
415 in lower CAPE values compared to that of the pre-monsoon. During post-monsoon, the mean
416 value of CAPE is about $\sim 1200 \text{ J kg}^{-1}$ except AS where it is about $\sim 1800 \text{ J kg}^{-1}$ and BoB
417 about $\sim 1500 \text{ J kg}^{-1}$. The northeast monsoon dominates the Indian region during post-monsoon
418 which results in deep convection resulting in relatively higher values of CAPE. Overall, the
419 maximum CAPE is found in the pre-monsoon followed by the post-monsoon, monsoon and
420 winter over the Indian sub-continent.

421

422 **5. Summary**

423 The extreme weather events such as thunderstorms and tropical cyclones cause severe
424 damage to life and property, especially in the tropical regions. Convective available potential
425 energy (CAPE) is a measure of the amount of energy available for convection in the
426 atmosphere. Hence, CAPE can be used as a measure for the occurrence of these severe
427 weather conditions. In the present study, we made an attempt for the first time to estimate
428 CAPE from the INSAT-3D measurements and evaluate comprehensively over the Indian sub-
429 continent. For the evaluation, 20 stations are selected in different parts of India and these
430 estimates are evaluated against the radiosonde measurements collected from the Wyoming
431 University along with the ERA-Interim data. The station wise comparison shows that the
432 INSAT-3D estimates match well with higher correlation coefficient and lower bias with the
433 radiosonde measurements. The correlation coefficient between INSAT-3D and radiosonde
434 CAPE is higher than that between INSAT-3D and ERA-Interim. Further, the INSAT-3D
435 derived CAPE overestimate the radiosonde CAPE, whereas the ERA-Interim underestimate
436 the radiosonde CAPE. The categorical statistics shows that the INSAT-3D can better
437 represent the radiosonde measured CAPE. The distribution of CAPE is higher for lower
438 values ($< 1000 \text{ J kg}^{-1}$) in all the three datasets (radiosonde, INSAT-3D and ERA-Interim) for

439 all the stations. The INSAT-3D and ERA-Interim estimated CAPE is higher than the
440 radiosonde measurements in the lower ranges. The INSAT-3D estimated CAPE matches well
441 with the radiosonde measurements above $\sim 3000 \text{ J kg}^{-1}$.

442 The spatial and temporal distribution of CAPE reveals that the weak instability is
443 predominant during winter season, moderate instability is higher during post-monsoon, strong
444 instability is more during monsoon period and extreme instability is higher during pre-
445 monsoon months. The diurnal variation in mean CAPE shows a bimodal distribution with
446 primary peak around mid-night and secondary peak in the afternoon times for most of the
447 regions and in different seasons. The seasonal mean CAPE shows that the land areas show
448 lower CAPE during winter, whereas the oceans show the highest CAPE during pre-monsoon
449 season. The higher values of CAPE over the oceanic regions may be due to higher occurrence
450 of the tropical cyclones during the pre-monsoon season. Further, the north-western parts of
451 India show higher CAPE among other land regions. Overall, the INSAT-3D estimated CAPE
452 is in close agreement with the radiosonde derived CAPE. As the INSAT-3D provides high
453 temporal and spatial resolution data, hence it can be used for nowcasting and severe weather
454 warnings in the numerical prediction models.

455

456 **Acknowledgement**

457 The authors sincerely acknowledge the Director, IITM for his constant support and
458 encouragement during this study. The authors would like to acknowledge Meteorological and
459 Oceanographic Satellite Data Archival Centre (MOSDAC) of Space Application Centre
460 (SAC), ISRO for supplying the INSAT-3D data. The authors are grateful to the Department
461 of Atmospheric Science, University of Wyoming for access to their radiosonde data archive.
462 The authors acknowledge the ERA-Interim team for providing their data. All the dataset are
463 freely available and can be downloaded from their respective archive. The authors would like

464 to sincerely thank the Editor and two anonymous reviewers for their insightful comments that
465 improved the quality of the manuscript.

466 **References:**

- 467 Arakawa, A. and Schubert, W. H.: Interaction of a Cumulus Cloud Ensemble with the Large-
468 Scale Environment, Part I, *J. Atmos. Sci.*, 31(3), 674–701, doi:10.1175/1520-
469 0469(1974)031<0674:IOACCE>2.0.CO;2, 1974.
- 470 Bevington, P. R., Robinson, D. K.: *Data reduction and Error Analysis for the Physical*
471 *Sciences*. McGraw-Hill, New York, 1992.
- 472 Brooks, H. E.: Severe thunderstorms and climate change, *Atmos. Res.*, 123(Supplement C),
473 129–138, doi:<https://doi.org/10.1016/j.atmosres.2012.04.002>, 2013.
- 474 Das, S. K., Konwar, M., Chakravarty, K. and Deshpande, S. M.: Raindrop size distribution of
475 different cloud types over the Western Ghats using simultaneous measurements from
476 Micro-Rain Radar and disdrometer, *Atmos. Res.*, 186, 72–82,
477 doi:<http://dx.doi.org/10.1016/j.atmosres.2016.11.003>, 2017.
- 478 de Coning, E., Koenig, M. and Olivier, J.: The combined instability index: A new very-short
479 range convection forecasting technique for southern Africa, *Meteorol. Appl.*, 18(4),
480 421–439, doi:10.1002/met.234, 2011.
- 481 Dee, D. P., Uppala, S. M., Simmons, A. J., Berrisford, P., Poli, P., Kobayashi, S., Andrae, U.,
482 Balmaseda, M. A., Balsamo, G., Bauer, P., Bechtold, P., Beljaars, A. C. M., van de
483 Berg, L., Bidlot, J., Bormann, N., Delsol, C., Dragani, R., Fuentes, M., Geer, A. J.,
484 Haimberger, L., Healy, S. B., Hersbach, H., Hólm, E. V, Isaksen, L., Kållberg, P.,
485 Köhler, M., Matricardi, M., McNally, A. P., Monge-Sanz, B. M., Morcrette, J.-J., Park,
486 B.-K., Peubey, C., de Rosnay, P., Tavolato, C., Thépaut, J.-N. and Vitart, F.: The ERA-
487 Interim reanalysis: configuration and performance of the data assimilation system, *Q. J.*
488 *R. Meteorol. Soc.*, 137(656), 553–597, doi:10.1002/qj.828, 2011.

489 DeMott, C. A. and Randall, D. A.: Observed variations of tropical convective available
490 potential energy, *J. Geophys. Res. Atmos.*, 109(D2), n/a–n/a,
491 doi:10.1029/2003JD003784, 2004.

492 Dhaka, S. K., Sapra, R., Panwar, V., Goel, A., Bhatnagar, R., Kaur, M., Mandal, T. K., Jain,
493 A. R. and Chun, H.-Y.: Influence of large-scale variations in convective available
494 potential energy (CAPE) and solar cycle over temperature in the tropopause region at
495 Delhi (28.3°N, 77.1°E), Kolkata (22.3°N, 88.2°E), Cochin (10°N, 77°E), and
496 Trivandrum (8.5°N, 77.0°E) using radiosonde during 1980–2005, *Earth, Planets Sp.*,
497 62(3), 319–331, doi:10.5047/eps.2009.09.001, 2010.

498 Donner, L. J. and Phillips, V. T.: Boundary layer control on convective available potential
499 energy: Implications for cumulus parameterization, *J. Geophys. Res. Atmos.*, 108(D22),
500 n/a–n/a, doi:10.1029/2003JD003773, 2003.

501 Dutta, S. N., and Kesarkar, A.P.: Diurnal and spatial variation of convective parameters over
502 Bay of Bengal during BOBMEX 1999, 2(April), 323–328, 2004.

503 Dutta, S. N., and Rao, G.S.P.: Diurnal and spatial variation of stability parameters at coastal
504 stations along the East Coast, during BOBMEX- 1999 , Proceedings of the TROPMET
505 2001 Symposium, 336-346, 2001.

506 Gaffen, D. J., Barnett, T. P. and Elliott, W. P.: Space and Time Scales of Global Tropospheric
507 Moisture, *J. Clim.*, 4(10), 989–1008, doi:10.1175/1520-
508 0442(1991)004<0989:SATSOG>2.0.CO;2, 1991.

509 Gartzke, J., Knuteson, R., Przybyl, G., Ackerman, S. and Revercomb, H.: Comparison of
510 Satellite-, Model-, and Radiosonde-Derived Convective Available Potential Energy in
511 the Southern Great Plains Region. *J. Appl. Meteor. Climatol.*, **56**, 1499–
512 1513, <https://doi.org/10.1175/JAMC-D-16-0267.1>, 2017.

513 Gettelman, A., Seidel, D. J., Wheeler, M. C. and Ross, R. J.: Multidecadal trends in tropical
514 convective available potential energy, *J. Geophys. Res. Atmos.*, 107(D21), ACL 17–1–
515 ACL 17–8, doi:10.1029/2001JD001082, 2002.

516 Jewett, C. P. and Mecikalski, J. R.: Estimating convective momentum fluxes using
517 geostationary satellite data, *J. Geophys. Res. Atmos.*, 115(14), 1–13,
518 doi:10.1029/2009JD012919, 2010.

519 Johns, R. H. and Doswell, C. A.: Severe Local Storms Forecasting, *Weather Forecast.*, 7(4),
520 588–612, doi:10.1175/1520-0434(1992)007<0588:SLSF>2.0.CO;2, 1992.

521 Koenig, M. and de Coning, E.: The MSG Global Instability Indices Product and Its Use as a
522 Nowcasting Tool, *Weather Forecast.*, 24(1), 272–285,
523 doi:10.1175/2008WAF2222141.1, 2009.

524 Lee, M.-I., Schubert, S. D., Suarez, M. J., Held, I. M., Kumar, A., Bell, T. L., Schemm, J.-K.
525 E., Lau, N.-C., Ploshay, J. J., Kim, H.-K. and Yoo, S.-H.: Sensitivity to Horizontal
526 Resolution in the AGCM Simulations of Warm Season Diurnal Cycle of Precipitation
527 over the United States and Northern Mexico, *J. Clim.*, 20(9), 1862–1881,
528 doi:10.1175/JCLI4090.1, 2007.

529 Mitra, A. K., Bhan, S. C., Sharma, A. K., Kaushik, N., Parihar, S., Mahandru, R. and Kundu,
530 P. K.: INSAT-3D vertical profile retrievals at IMDPS , New Delhi : A preliminary
531 evaluation operational High resolution Infrared Radiation Sounder, 4(October), 687–
532 694, 2015.

533 Moncrieff, M. W. and Miller, M. J.: The dynamics and simulation of tropical cumulonimbus
534 and squall lines, *Q. J. R. Meteorol. Soc.*, 102(432), 373–394,
535 doi:10.1002/qj.49710243208, 1976.

536 Murugavel, P., Pawar, S. D. and Gopalakrishnan, V.: Trends of Convective Available
537 Potential Energy over the Indian region and its effect on rainfall, *Int. J. Climatol.*, 32(9),
538 1362–1372, doi:10.1002/joc.2359, 2012.

539 Narendra Babu, A., Nee, J. B. and Kumar, K. K.: Seasonal and diurnal variation of
540 convective available potential energy (CAPE) using COSMIC/FORMOSAT-3
541 observations over the tropics, *J. Geophys. Res. Atmos.*, 115(D4), n/a–n/a,
542 doi:10.1029/2009JD012535, 2010.

543 Ratnam, M. V., Hemanth Kumar, A. and Jayaraman, A.: Validation of INSAT-3D sounder
544 data with in situ measurements and other similar satellite observations over India,
545 *Atmos. Meas. Tech.*, 9(12), 5735–5745, doi:10.5194/amt-9-5735-2016, 2016.

546 Raut, B. A., Karekar, R. N., and Puranik, D. M.: Spatial distribution and diurnal variation of
547 cumuliform clouds during Indian Summer Monsoon. *J. Geophys. Res. Atmos.*, 114(11),
548 1–12. <https://doi.org/10.1029/2008JD011153>, 2009.

549 Riemann-Campe, K., Fraedrich, K. and Lunkeit, F.: Global climatology of Convective
550 Available Potential Energy (CAPE) and Convective Inhibition (CIN) in ERA-40
551 reanalysis, *Atmos. Res.*, 93(1), 534–545,
552 doi:<https://doi.org/10.1016/j.atmosres.2008.09.037>, 2009.

553 Santhi, Y. D., Ratnam, M. V., Dhaka, S. K., and Rao, S. V.: Global morphology of
554 convection indices observed using COSMIC GPS RO satellite measurements. *Atmos.*
555 *Res.*, 137, 205–215. <https://doi.org/10.1016/j.atmosres.2013.10.002>, 2014.

556 Siewert, C. W., Koenig, M. and Mecikalski, J. R.: Application of Meteosat second generation
557 data towards improving the nowcasting of convective initiation, *Meteorol. Appl.*, 17(4),
558 442–451, doi:10.1002/met.176, 2010.

559 Uma, K. N. and Das, S. K.: Do the stability indices indicate the formation of deep
560 convection?, *Meteorol. Atmos. Phys.*, doi:10.1007/s00703-017-0550-9, 2017.

- 561 Uma, K. N. and Das, S. S.: Quantitative and qualitative assessment of diurnal variability in
562 tropospheric humidity using SAPHIR on-board Megha-Tropiques, *J. Atmos. Solar-*
563 *Terrestrial Phys.*, 146(Supplement C), 89–100,
564 doi:<https://doi.org/10.1016/j.jastp.2016.05.009>, 2016.
- 565 Utsav, B., Deshpande, S. M., Das, S. K. and Pandithurai, G.: Statistical Characteristics of
566 Convective Clouds over the Western Ghats Derived from Weather Radar Observations,
567 *J. Geophys. Res. Atmos.*, 122(18), 10,10–50,76, doi:10.1002/2016JD026183, 2017.
- 568 Washington, W. M. and Parkinson, C. L.: Introduction to three-dimensional climate
569 modeling, University Science Books, Mill Valley, CA, United States, 2005.

570 **Table Captions:**

571 **Table 1:** The total number of data available during four seasons for the 20 stations for the
572 period from April 2014 to March 2017.

573 **Table 2:** Contingency table for the comparison of INSAT-3D estimated CAPE with
574 radiosonde measured CAPE. The CAPE threshold is considered as 0 J kg^{-1} .

575

576 **Figure Captions:**

577 **Fig 1:** The geographical map of India representing the 20 stations considered for the present
578 study.

579 **Fig 2:** (a) Correlation coefficient in the comparison of INSAT-3D CAPE with radiosonde
580 and ERA-Interim CAPE for 20 stations in India for the period April 2014 to March
581 2017. (b) Number of data points in the comparison of INSAT-3D CAPE with
582 radiosonde and ERA-Interim CAPE.

583 **Fig 3:** Bias in the comparison between INSAT-3D CAPE and ERA-Interim reanalysis CAPE
584 with radiosonde for different stations in India for the period April 2014 – March
585 2017.

586 **Fig 4:** Statistical indices (a) POD, (b) FAR, (c) CSI and (d) ACC in the comparison between
587 the INSAT-3D CAPE with radiosonde CAPE for 20 stations in India.

588 **Fig 5:** Distribution (%) of INSAT-3D, radiosonde and ERA-Interim reanalysis CAPE (J kg^{-1})
589 for all the stations considered in the study.

590 **Fig. 6:** The distribution of CAPE (J kg^{-1}) during (a) winter (b) pre-monsoon (c) monsoon and
591 (d) post-monsoon from INSAT-3D data over Indian region.

592 **Fig. 7:** Frequency distribution (%) of CAPE in (a) weak (b) moderate (c) strong (d) extreme
593 instability during winter season. (e)-(h): same as (a)-(d) except for pre-monsoon

594 season. (i)-(l): same as (a)-(d) but for monsoon season and (m)-(p): same as (a)-(d)
595 except for post-monsoon season.

596 **Fig 8:** Hourly mean distribution of INSAT-3D CAPE (J kg^{-1}) during the period from 01 April
597 2014 to 31 March 2017 over the Indian region.

598 **Fig 9:** Diurnal variation of CAPE (J kg^{-1}) over (a) AS (b) BoB (c) SP (d) CI (e) NI (f) NE
599 region of India during four seasons.

600 **Fig 10:** Box-plot analysis of CAPE (J kg^{-1}) during (a) winter (b) pre-monsoon (c) monsoon
601 and (d) post-monsoon from INSAT-3D data over six sub-regions over the Indian
602 sub-continent.

603 **Table 1:** The total number of data available during four seasons for the 20 stations for the
 604 period from April 2014 to March 2017.

Station	Latitude	Longitude	Total Number of Data			
			Winter	Pre- monsoon	Monsoon	Post- monsoon
Agarthala (AGR)	23.88	91.25	3614	3272	2615	2613
Ahmedabad (AHB)	23.06	72.63	3808	4034	3686	2891
Amini Divi (AMD)	11.12	72.73	3985	3776	3327	2362
Bhuvanesar (BHU)	20.25	85.83	3701	3450	2389	2488
Chennai (CHE)	13.00	80.18	3816	3712	2956	1985
Cochin (COC)	9.95	76.26	3867	3072	2905	1758
Delhi (DEL)	28.58	77.20	2910	3316	3845	2894
Dibrugarh (DIB)	27.48	95.01	3287	2260	2536	2595
Gorakhpur (GRK)	26.75	83.36	2871	3383	2769	2833
Guwahati (GUW)	26.10	91.58	3610	3058	2956	2796
Hyderabad (HYD)	17.45	78.46	2550	394	327	1045
Karaikal (KAR)	10.91	79.83	3660	3458	3632	1846
Kolkata (KOL)	22.65	88.45	3488	2924	2500	2677
Machilipatnam (MAP)	16.20	81.15	4001	3706	2564	2322
Mangalore (MAN)	12.95	74.83	4063	3542	2705	2232
Minicoy (MIN)	8.30	73.15	3882	3346	3320	2040

Mumbai (MUM)	19.11	72.85	4294	4321	3405	2756
Port Blair (PB)	11.66	92.71	3676	3458	2381	2178
Trivandrum (TVM)	8.48	76.95	3675	3116	3608	1805
Visakhapatnam (VSP)	17.70	83.30	3972	3747	2632	2415

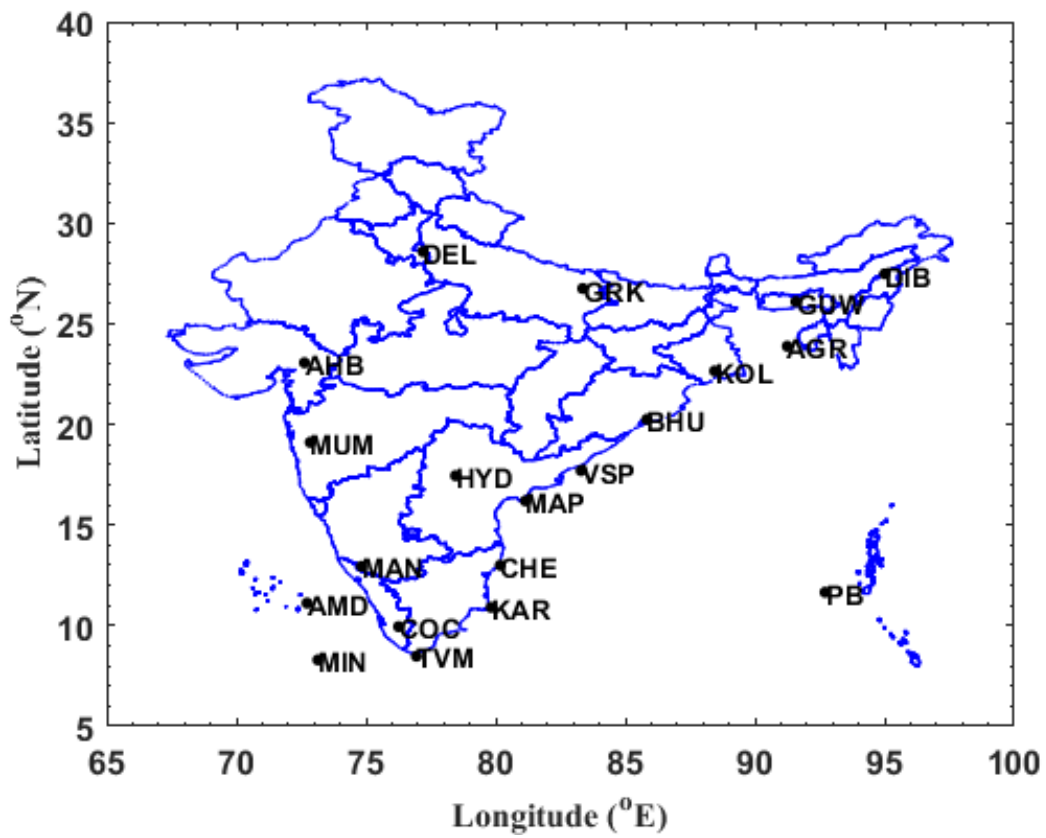
605

606 **Table 2:** Contingency table for the comparison of INSAT-3D estimated CAPE with
607 radiosonde measured CAPE. The CAPE threshold is considered as 0 J kg^{-1} .

	Radiosonde \geq Threshold	Radiosonde $<$ Threshold
Satellite \geq Threshold	Hits (a)	False alarms (b)
Satellite $<$ Threshold	Misses (c)	Correct negatives (d)

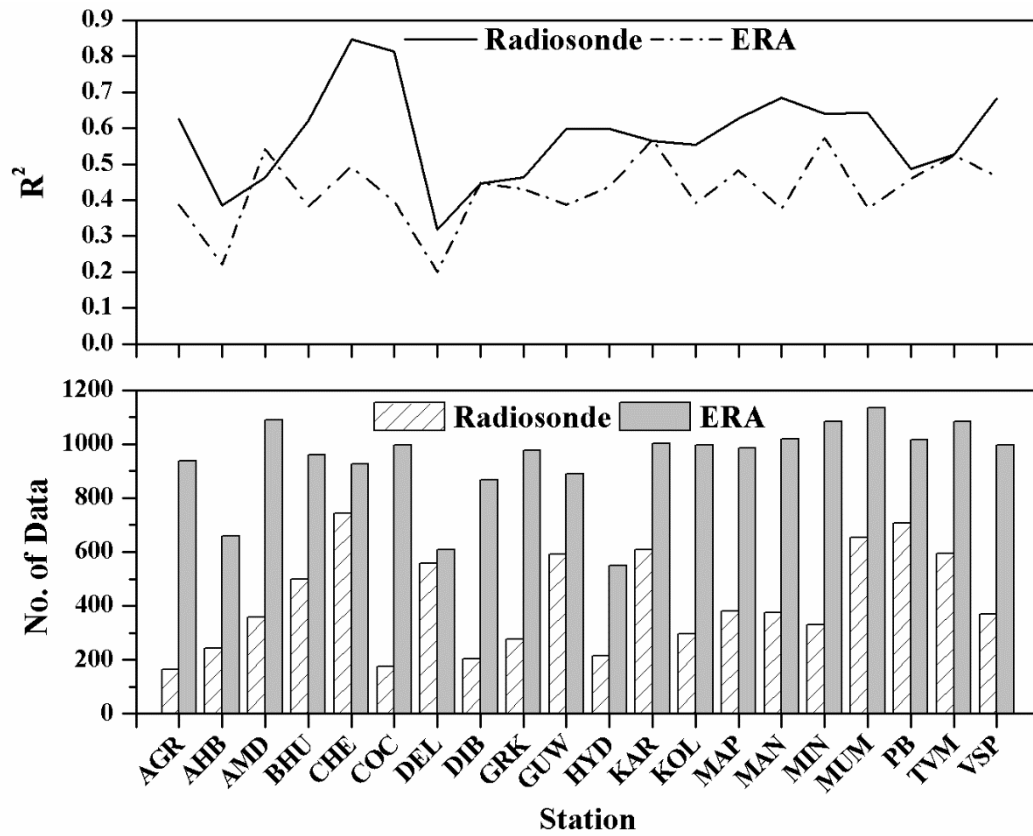
608

609



610

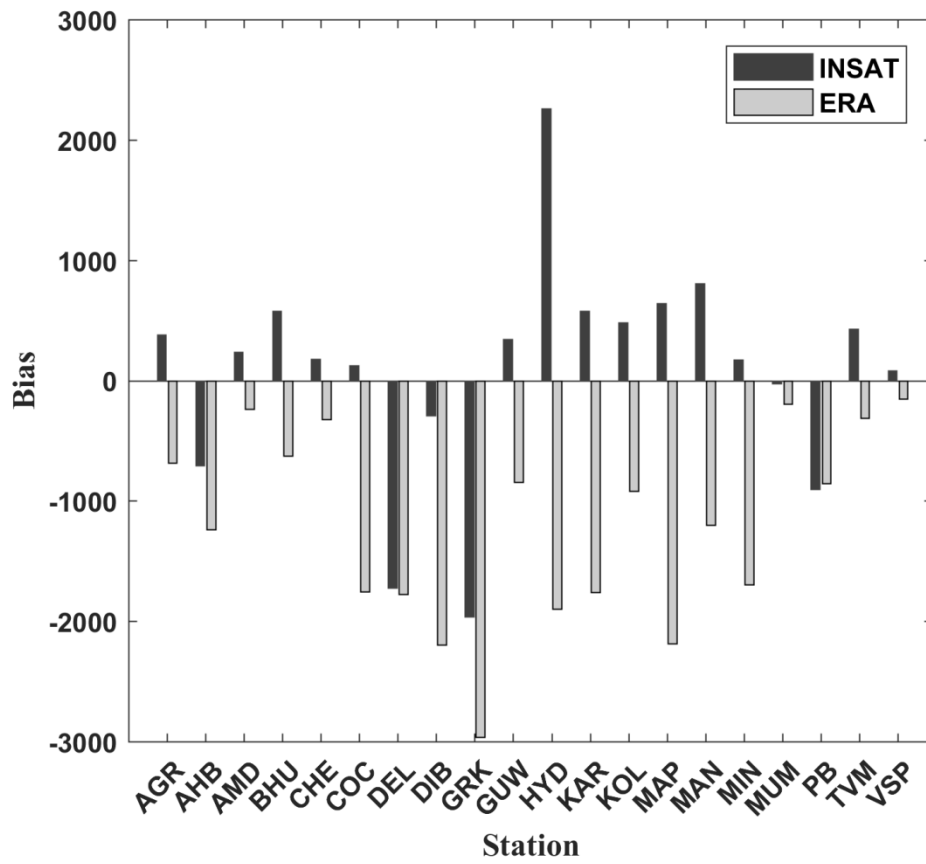
611 **Fig 1:** The geographical map of India representing the 20 stations considered for the present
 612 study.



613

614 **Fig 2:** (a) Correlation coefficient in the comparison of INSAT-3D CAPE with radiosonde
 615 and ERA-Interim CAPE for 20 stations in India for the period April 2014 to March
 616 2017. (b) Number of data points in the comparison of INSAT-3D CAPE with
 617 radiosonde and ERA-Interim CAPE.

618



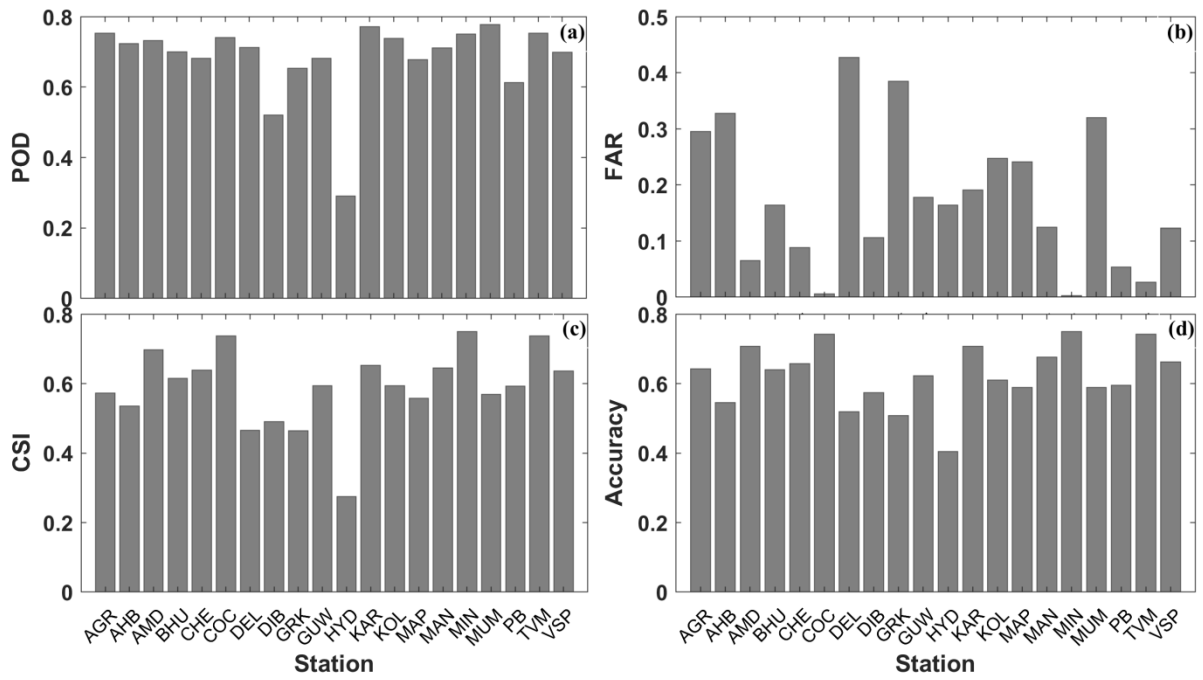
619

620 **Fig 3:** Bias in the comparison between INSAT-3D CAPE and ERA-Interim reanalysis CAPE

621 with radiosonde for different Stations in India for the period April 2014 – March

622 2017.

623

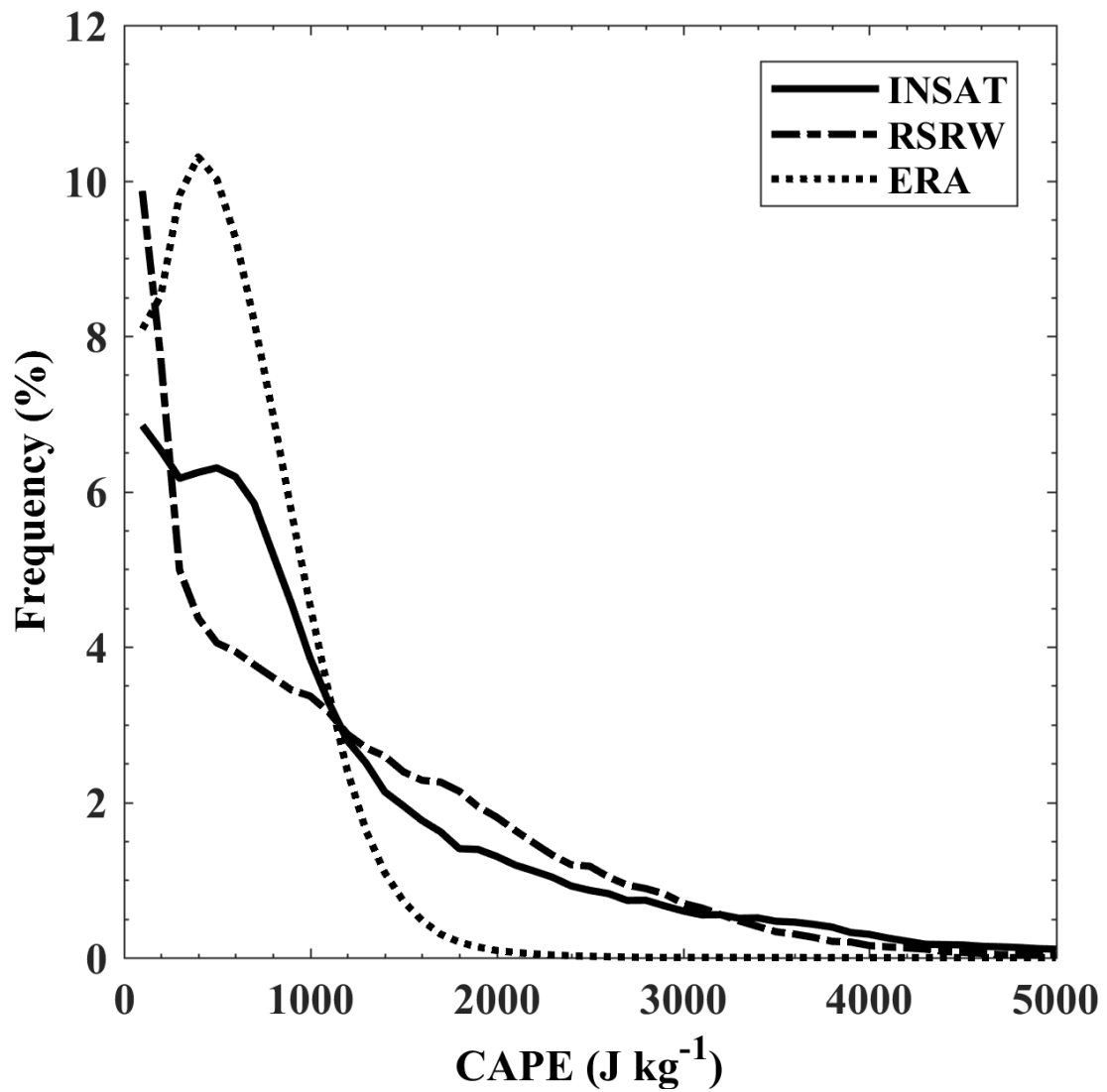


624

625 **Fig 4:** Statistical indices (a) POD, (b) FAR, (c) CSI and (d) ACC in the comparison between

626

the INSAT-3D CAPE with radiosonde CAPE for 20 stations in India.

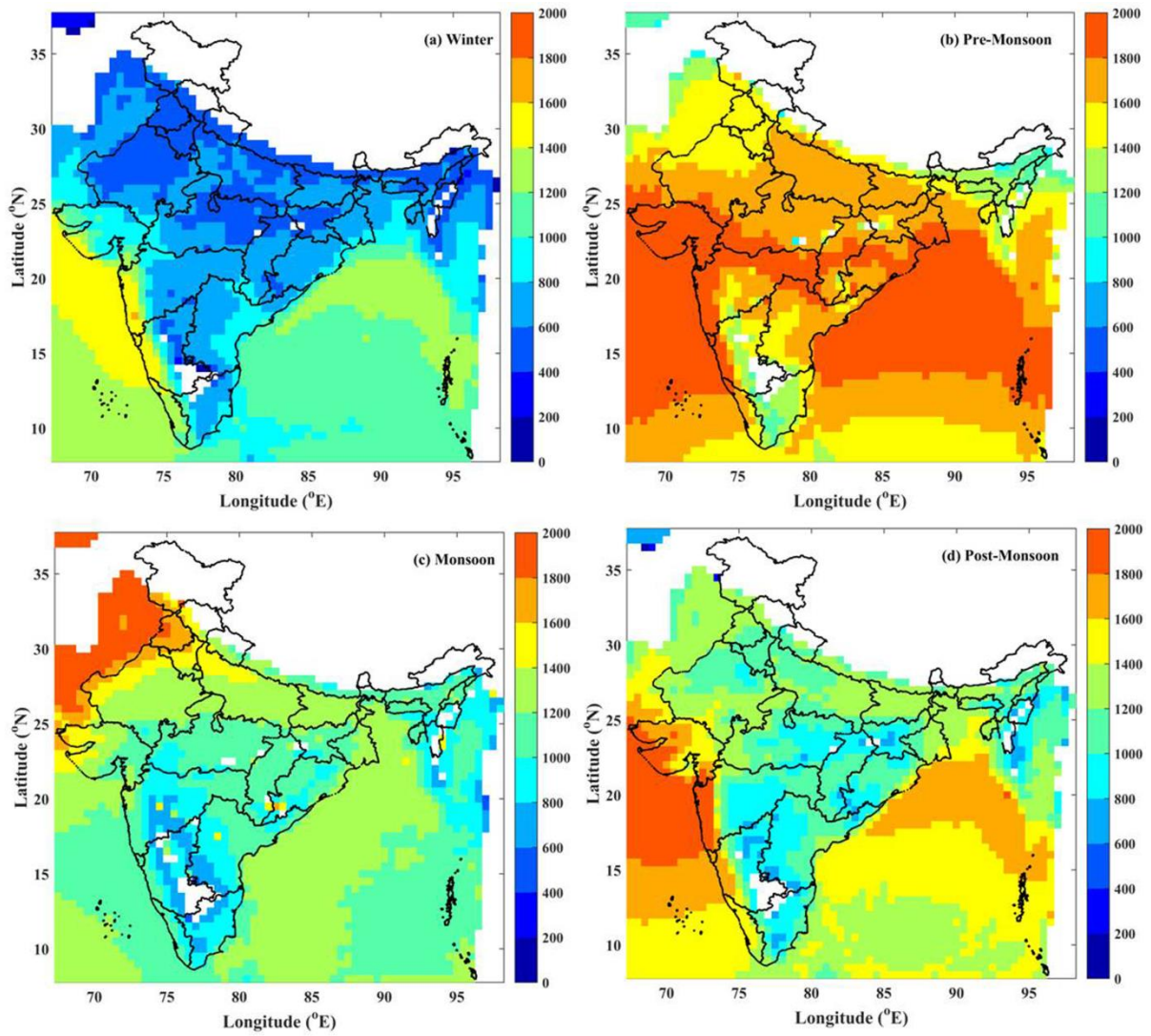


627

628 **Fig 5:** Distribution (%) of INSAT-3D, radiosonde and ERA-Interim reanalysis CAPE (J kg^{-1})

629

for all the stations considered in the study.

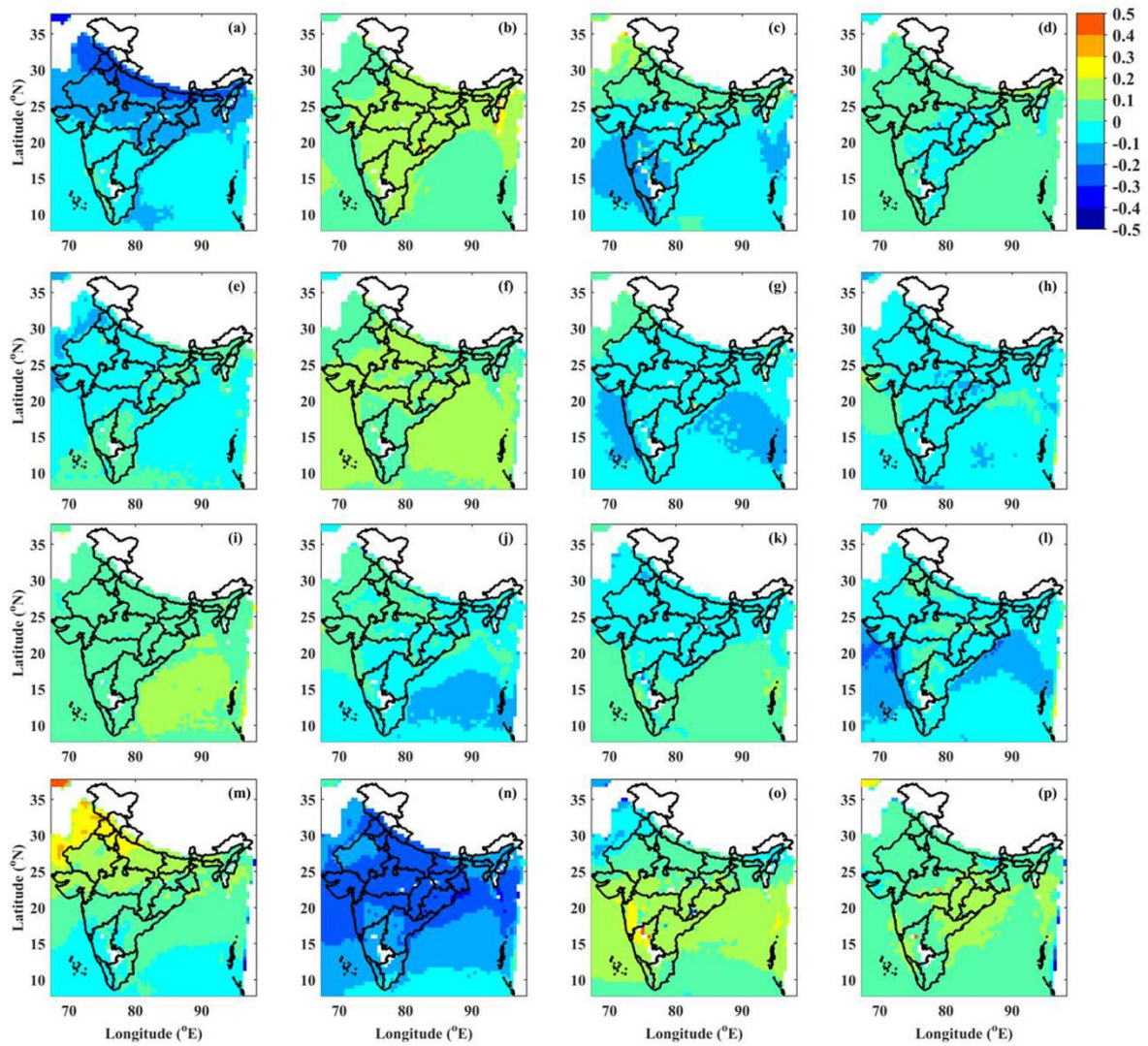


630

631 **Fig. 6:** The distribution of CAPE (J kg^{-1}) during (a) winter (b) pre-monsoon (c) monsoon and

632

(d) post-monsoon from INSAT-3D data over Indian region.



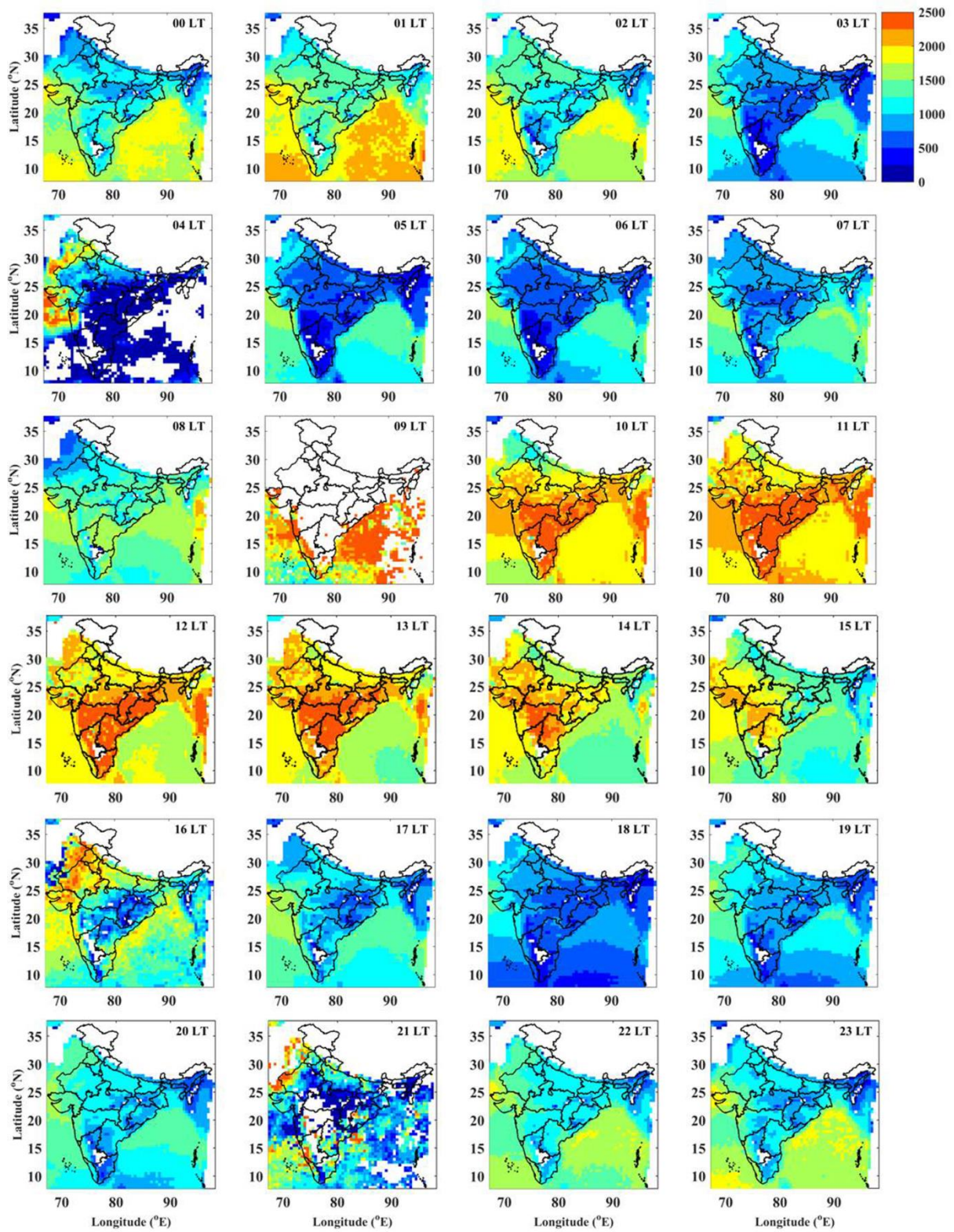
633

634 **Fig. 7:** Frequency distribution (%) of CAPE in (a) weak (b) moderate (c) strong (d) extreme

635 instability during winter season. (e)-(h): same as (a)-(d) except for pre-monsoon

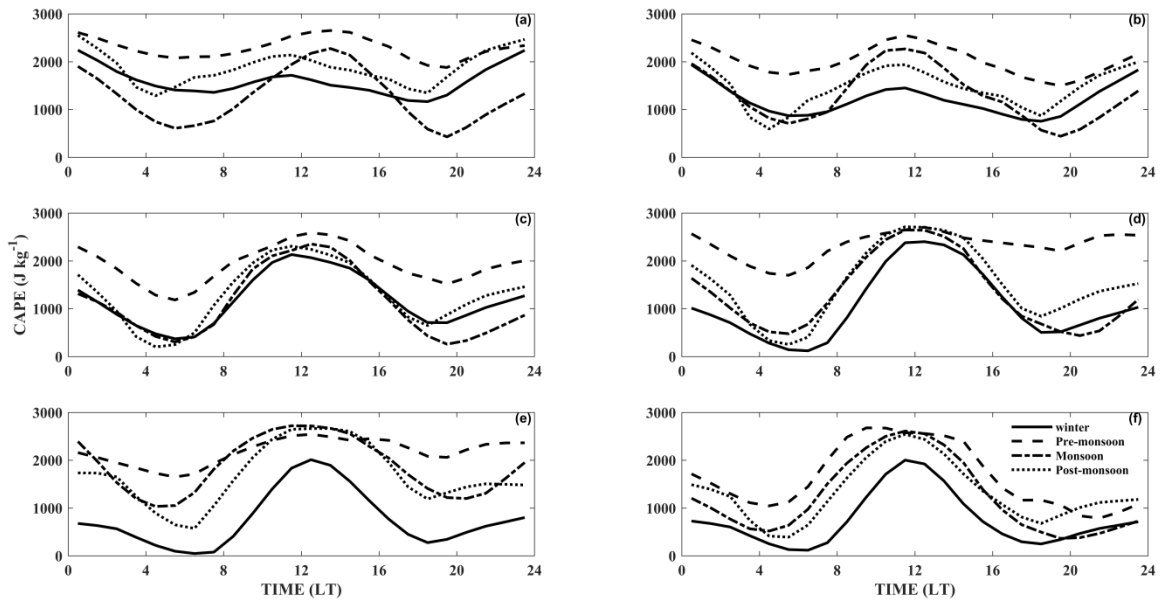
636 season. (i)-(l): same as (a)-(d) but for monsoon season and (m)-(p): same as (a)-(d)

637 except for post-monsoon season.



638

639 **Fig 8:** Hourly mean distribution of INSAT-3D CAPE (J kg^{-1}) during the period from 01 April
 640 2014 to 31 March 2017 over the Indian region.



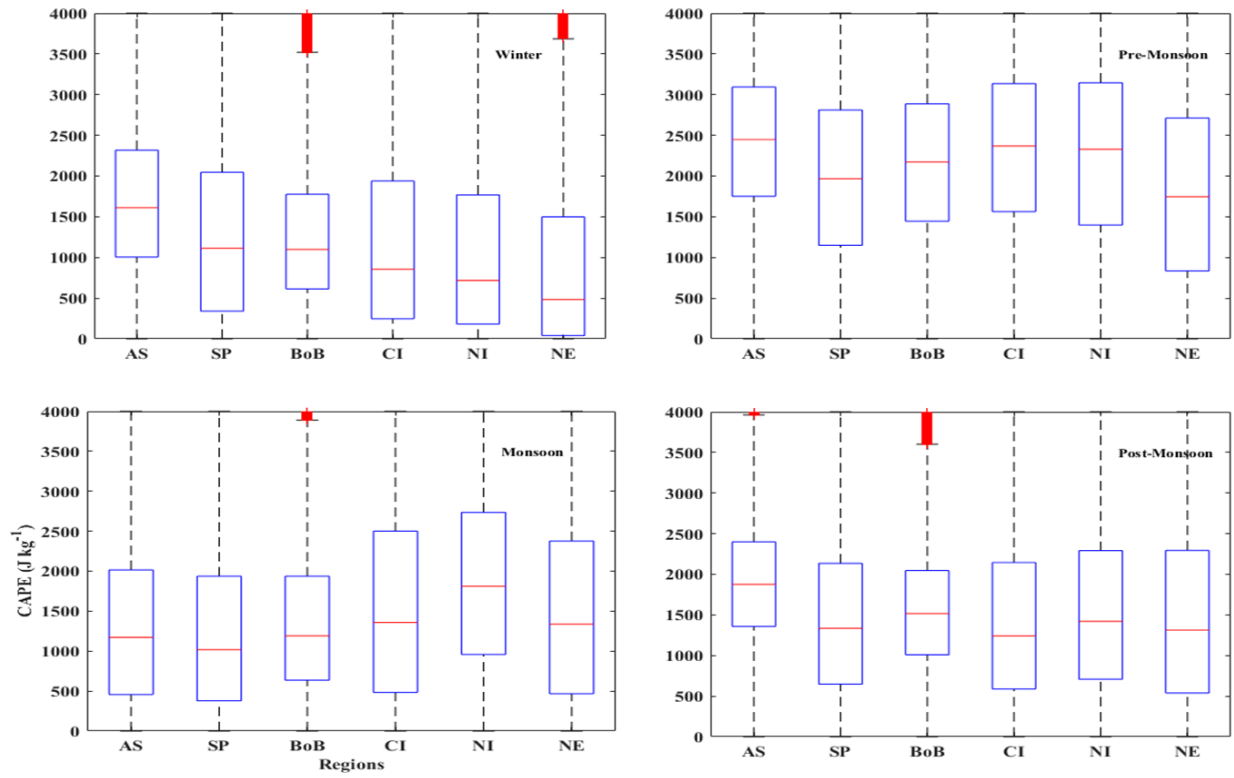
641

642 **Fig 9:** Diurnal variation of CAPE ($J\ kg^{-1}$) over (a) AS (b) BoB (c) SP (d) CI (e) NI (f) NE

643

region of India during four seasons.

644



645

646 **Fig 10:** Box-plot analysis of CAPE (J kg^{-1}) during (a) winter (b) pre-monsoon (c) monsoon
 647 and (d) post-monsoon from INSAT-3D data over six sub-regions over the Indian sub-
 648 continent.